NeuroImage **14,** 723–735 (2001)
doi:10.1006/nimg.2001.0861, available online at http://www.idealibrary.com on IDEAL®

Diffusion Tensor Imaging and Axonal Tracking in the Human Brainstem

Bram Stieltjes,*,† Walter E. Kaufmann,*,†,‡,§,¶ Peter C. M. van Zijl,*,¶ Kim Fredericksen,*,¶ Godfrey D. Pearlson,†,¶,‖ Meiyappan Solaiyappan,* and Susumu Mori*,¶,[1]

**Department of Radiology and Radiological Science; ‡Department of Pathology; §Department of Neurology; †Department of Psychiatry; ¶Kennedy Krieger Institute, F. M. Kirby Research Center for Functional Brain Imaging; and ‖Department of Mental Hygiene, Johns Hopkins University School of Medicine, 720 Rutland Avenue, Baltimore, Maryland 21205*

Received January 17, 2001; published online July 13, 2001

Diffusion tensor MRI was used to demonstrate *in vivo* anatomical mapping of brainstem axonal connections. It was possible to identify the corticospinal tract (CST), medial lemniscus, and the superior, medial, and inferior cerebellar peduncles. In addition, the cerebral peduncle could be subparcellated into component tracts, namely, the frontopontine tract, the CST, and the temporo-/parieto-/occipitopontine tract. Anatomical landmarks and tracking thresholds were established for each fiber and, using these standards, reproducibility of automated tracking as assessed by intra- and interrater reliability was found to be high ($\kappa > 0.82$). Reconstructed fibers corresponded well to existing anatomical knowledge, validating the tracking. Information on the location of individual tracts was coregistered with quantitative MRI maps to automatically measure MRI parameters on a tract-by-tract basis. The results reveal that each tract has a unique spatial signature in terms of water relaxation and diffusion anisotropy.

The brainstem is a region characterized by densely packed fibers traveling to and from the cerebrum and cerebellum (Carpenter, 1976). Some of these fibers, such as the corticospinal tract and the superior cerebellar peduncle, are of critical importance in the initiation, control, and execution of movement and are postulated to be involved in higher skills such as motor learning (Orioli and Strick, 1989). Others, such as the spinocerebellar tract and the inferior cerebellar peduncle, carry sensory information to the cerebellum (Yaginuma and Matsushita, 1989). Fiber bundles in the brainstem are involved in a wide spectrum of neurologic disorders, including amyotrophic lateral sclerosis, multiple sclerosis, leukodystrophies, cerebrovascular disease, and brain tumors. Thus, noninvasive *in vivo* visualization and delineation of the brainstem's white matter tracts would not only provide information about the normal neuroanatomy of brain connections, but also might improve the detection and further assessment of many neurologic conditions. However, conventional radiological techniques including MRI often lack appropriate contrast to discretely delineate white matter components of the brainstem and, as a result, their diagnostic value for the aforementioned disorders is far from optimum.

Diffusion tensor imaging (DTI) is a technique that can characterize the spatial properties of molecular diffusion processes (Basser *et al.,* 1994a,b; van Gelderen *et al.,* 1994; Mori and van Zijl, 1995). The application of this technique to the central nervous system has revealed that the diffusion of water in white matter is anisotropic. This directionality has been attributed to constraints imposed upon water motion by the ordered structure of axons and myelin sheaths (Moseley *et al.,* 1990; Beaulieu and Allen, 1994; Henkelman *et al.,* 1994; Pierpaoli *et al.,* 1996). Using DTI, both the magnitude of anisotropy and the orientation in which water preferentially diffuses can be quantified. By combining these two parameters, anisotropy and orientation, DTI provides new and unique opportunities for studying the white matter architecture. In this study, we explore the capabilities of several types of emerging DTI methods and analyses to study fiber pathways in the human brainstem *in vivo.* One is the so-called color-coded map (Douek *et al.,* 1991; Coremans *et al.,* 1994; Nakada and Matsuzawa, 1995; Makris *et al.,* 1997; Pajevic and Pierpaoli, 1999), which provides a template of white matter architecture based on measurements of anisotropy and orientation. Another is the three-dimensional tracking of axonal projections (Mori *et al.,* 1999, 2000; Xue *et al.,* 1999; Conturo *et al.,* 1999; Basser *et al.,* 2000; Poupon *et al.,* 2000). Fiber bundles delineated by either color-coded

[1] To whom reprint requests should be addressed. School of Medicine, Department of Radiology, Johns Hopkins University, 217 Traylor Building, 720 Rutland Avenue, Baltimore, MD 21205. Fax: (410) 614-1948. E-mail: susumu@mri.jhu.edu.

1053-8119/01 $35.00

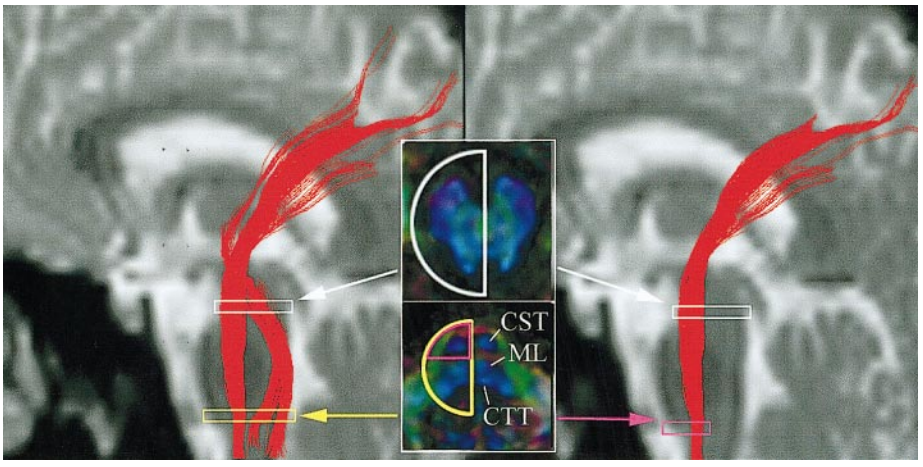

FIG. 1. Effect of location and size of the reference ROI on the reconstruction of the corticospinal tract. CST, corticospinal tract; ML, medial lemniscus; CTT, central tegmental tract.

maps or tracking approaches can also be examined in terms of MR properties. In this paper, we perform such a 3D-guided quantitative analysis of MR parameters of white matter on a tract-by-tract basis. We selected the brainstem as the region for applying these methods for several reasons. First, compared to the cerebral hemispheres, many of the tracts have relatively simple trajectories with few branches. Second, there is accumulated knowledge on the trajectories of these fibers based on postmortem anatomical studies. These advantages make the brainstem particularly suitable for the implementation and validation of DTI techniques. Using these types of DTI analyses described above, we were able to delineate the corticospinal tract, the medial lemniscus, and the superior, medial, and inferior cerebellar peduncles in normal young adults. In addition, the cerebral peduncle was parcellated into its the fiber system components. Finally, quantification of MRI parameters on individual tracts revealed that each brainstem bundle has a unique spatial signature in terms of water relaxation and diffusion anisotropy.

MATERIALS AND METHODS

MRI Data Acquisition

Six healthy, right-handed volunteers (three males, three females), aged 22 to 32 (mean age 27) years participated in this study. All studies were performed using a 1.5-T Philips Gyroscan NT system. RF excitation on this system is performed using the body coil, leading to a highly homogeneous B1 field over all cerebral and brainstem areas. Reception is with a head coil. Diffusion-weighted imaging was accomplished using multislice segmented echoplanar imaging (EPI), with cardiac triggering and navigator echo phase correction (motion correction) (Ordidge *et al.*, 1994). A data matrix of 64 × 64 over a field of view of 120 × 120 mm was obtained using acquisition of 17 echoes per excitation. Imaging slices were positioned to make the slice perpendicular to the longitudinal axis of the brainstem at the pons level. Slice thickness was 3 mm without a gap (40 slices); TE = 92 ms; TR = 5 heart beats; *k*-space data were zerofilled to a resolution of 1 × 1 × 3 mm before Fourier transform to image space. Diffusion weighting was performed along six independent axes, using diffusion weighting of $b = 600$ s/mm^2 at the maximum gradient strength of 2.1 G/cm. A reference image with low diffusion weighting ($b = 33$ s/mm^2) was also recorded. A single set of these seven measurements took about 4–5 min depending on the heart rate. Measurements were repeated six times to increase signal to noise. Double-echo T_2-weighted imaging (TEs of 22 and 100 ms; image resolution equal to DTI) was also performed for anatomical guidance and T_2 quantification. The entire examination was completed within 50 min. To ensure coregistration of the T_2 and DTI images, the same data acquisition scheme (EPI with 17-echo acquisition) was used for the double-echo imaging.

The brain tumor patient was a 41-year-old woman with a parasellar meningoma, diagnosed 7 years before scanning. Her clinical presentation was characterized by intermittently disturbed balance, temporary loss of voice and difficulties with swallowing. She also had minor disturbances in eye movements.

Data Processing

Data were processed on a SUN Enterprise computer. Images were first realigned using the AIR program (Woods *et al.*, 1992), in order to remove any potential small bulk motions that occurred during the scans. Subsequently, all individual images were visually inspected to discard slices with motion artifacts. This process was needed because, in spite of the navigator-echo-based motion correction, image corruption can occur due to motion during the scan. On average, the fraction of the discarded images in this study was 2.8 ±

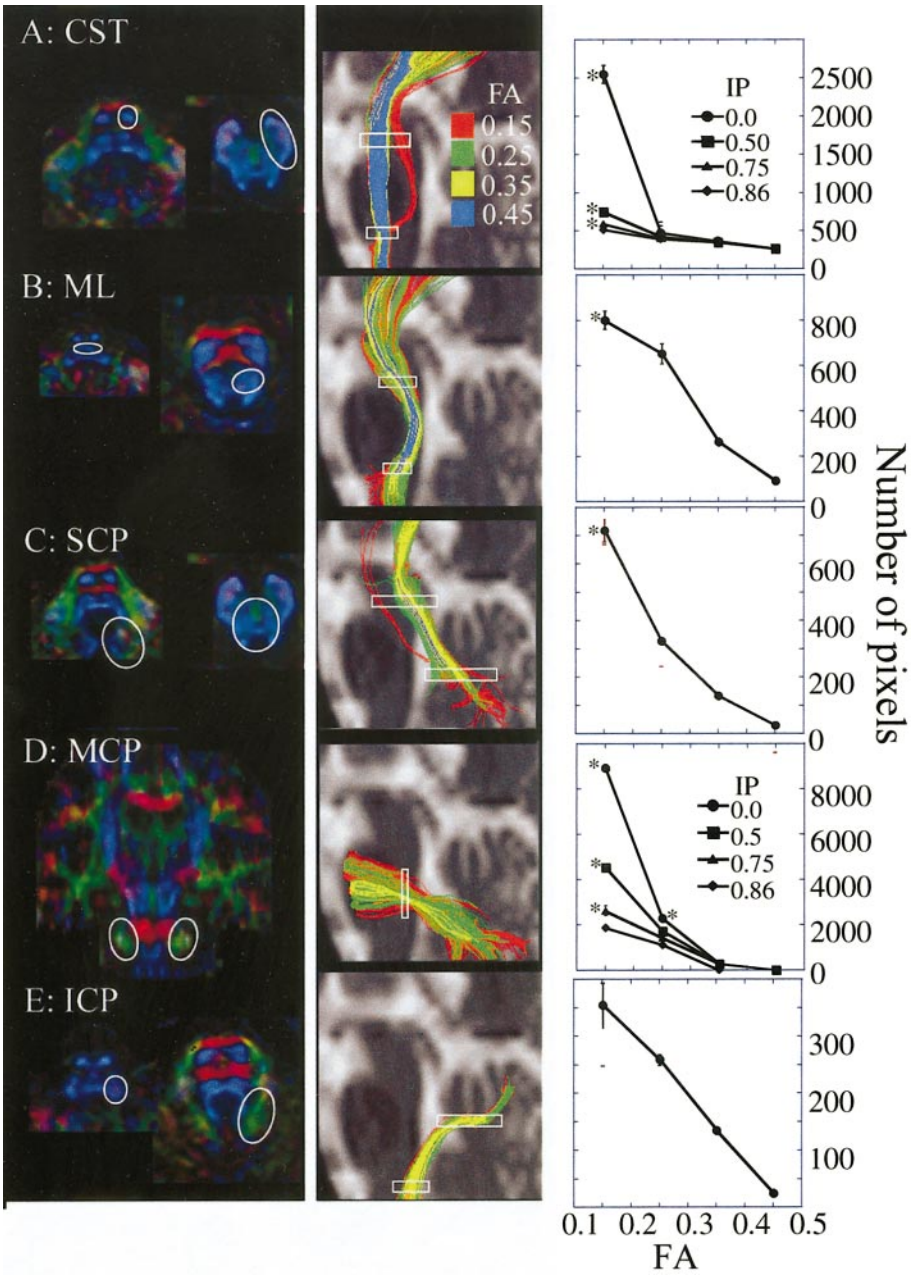

FIG. 2. Locations of the anatomical reference ROIs on the DTI color map (left column) and with respect to the final tracking projected on the sagittal plane (middle column). The effect of FA (middle and right column) and IP (right column) threshold values is shown for five major tracts (A–E; specified in figure) with respect to tracking (middle column) and number of pixels (right column) included in the tracts. White boxes in the middle column indicate slice locations of the reference ROIs. The different tract colors in the middle column correspond to different tracking results for various FA threshold values. Results in the right column are the averages and standard deviations of three tracking results performed by the same rater. Asterisks in the graphs indicate that the results contained contamination by other tracts.

2.1% (SD) for the six subjects. This is a small fraction and we do not expect it to influence signal to noise sufficiently to significantly alter anisotropy and eigenvector values. After the image quality check, the pixel intensities of the multiple diffusion-weighted images were fitted using multivariant linear least square fitting to obtain the six elements of the symmetric diffusion tensor (Basser *et al.*, 1994). The diffusion tensors at each pixel were diagonalized to obtain eigenvalues and eigenvectors for each pixel. The eigenvector (v_1) associated with the largest eigenvalue (λ_1) was assumed to represent the local fiber direction. Anisotropy maps were obtained using the orientation-independent fractional anisotropy (FA) (Pierpaoli and Basser, 1996). DTI-based color maps were created from FA values and the three vector elements of $\overline{v_1}$. Vector elements were assigned to red (x element, left–right), green (y, anterior–posterior), and blue (z, superior–

inferior) (Makris *et al.*, 1997; Pajevic and Pierpaoli, 1999). The intensities of the maps were scaled in proportion to the FA.

Fiber Tracking and Quantitative Analyses

Fiber tracking was performed automatically using our previously described FACT method (Mori *et al.*, 1999; Xue *et al.*, 1999) and a range of different threshold values for the anisotropy and the inner product (*IP*) between the two eigenvectors to be connected by the tracking. *IP* is a measure of the angle (inverse relationship) between two connected vectors, and is defined as

$$IP = \overline{V1i} \cdot \overline{V1j}$$

(i and *j* are indices of two connected pixels).

Briefly, tracking was initiated from a seed pixel from which a line was propagated in both retrograde and orthograde directions according to $\overline{v_1}$ at each pixel. Tracking was terminated when it reached a pixel with FA and/or *IP* lower than certain thresholds. These thresholds were first varied and subsequently evaluated on the basis of the tracking results. There were two strategies for initiation of tracking. One was to begin tracking from each pixel included in the regions of interest (ROI). This approach could delineate only a limited number of branching patterns of the tract of interest (e.g., if the ROI contains 10 pixels, there are only 10 tracking results to delineate the tract). In the second method, fiber tracking was initiated from the center of every single pixel in the brain, but only fibers passing through chosen reference ROIs were retained (Conturo *et al.*, 1999). In this approach, multiple tracking results penetrated the ROI, thus revealing a more comprehensive tract structure. In this study, we used the latter approach. Based on anatomical knowledge of the fiber projections in relation to landmarks, we defined multiple ROI. This principle is illustrated in Fig. 1 for the tracking of the CST. Because the CST is known to be a dominant pathway that penetrates the entire brainstem, two large ROIs can be placed at the midbrain and the lower pons level that include the entire right half of the brain. The FACT method then was applied from the center of all pixels in the brain to find all tracts that penetrate these two ROIs. For this example, thresholds for FA and IP were set at 0.35 and 0.75, respectively. The results in Fig. 1 (left) indicate that the choice of these two large ROIs identifies several combined pathways, namely, the CST, medial lemniscus (ML), and other tracts, possibly the central tegmental tract and/or the medial longitudinal fasciculus (CTT/MLF). Figure 1 (right) shows the result when the second ROI was changed to exclude ML and CTT/MLF, thereby reconstructing only the CST. Quantitative analyses of size and MRI properties of individual tracts were done on the basis of the established thresholds for the 3D tracking results by superimposing the fiber trajectories on coregistered FA and T_2 maps.

Statistical Analysis

For statistical analysis of intra- and interrater reproducibility (reliability), two tracking results performed using the same data set were spatially superimposed. This combined image identified four groups of pixels: (1) pixels that did not contain the tract (nn), (2) pixels that contained the tract in only one of the two results (pn, np), and (3) pixels that contained the tracts in both of the results (pp). Expected values for each class were then calculated using the equations

$$\text{Expected nn (Enn)} = (\text{nn} + \text{np})(\text{nn} + \text{pn})/N$$

$$\text{Expected np (Enp) or Epn} = (\text{nn} + \text{np})(\text{np} + \text{pp})/N \text{ or } (\text{nn} + \text{pn})(\text{pn} + \text{pp})/N$$

$$\text{Expected pp (Epp)} = (\text{pn} + \text{pp})(\text{np} + \text{pp})/N,$$

where $N = \text{nn} + \text{np} + \text{pn} + \text{pp}$ is the total number of pixels. Then κ can be determined by

$$\kappa = (\text{observed agreement} - \text{expected agreement})/(100 - \text{expected agreement})$$

where

$$\text{observed agreement} = (\text{nn} + \text{pp})/N * 100$$

$$\text{expected agreement} = (\text{Enn} + \text{Epp})/N * 100.$$

According to criteria set by Landis and Koch (1977), the κ value of 0.01–0.2 is considered as "slight," 0.21–0.4 as "fair," 0.41–0.60 as "moderate," 0.61–0.80 as "substantial," and 0.81–1.0 as "almost perfect" agreement.

RESULTS

Effect of ROI Location and FA/IP Thresholds

In Fig. 2, the locations of reference ROIs that are optimized to identify each tract discretely are shown. Tracking of the CST was presented in Fig. 1. As long as the second reference ROI excluded the regions of the ML and CTT/MLF, and was drawn sufficiently large to contain the entire CST identifiable in the color map, the result was completely reproducible ($\kappa = 1.0$, five repeated measurements by the same operator). In practice, the first reference ROI at the midbrain level was always drawn to include only the cerebral peduncle, which could be discretely identified in the color map and is known to contain the CST as shown in Fig. 2A. For the ML, one ROI was placed at the medullar

level close to the decussation at the medulla level (Fig. 2B). Contamination by adjacent tracts, most notably, the CTT/MLF was avoided by excluding them from the ROI. For the SCP, one ROI was placed in the white matter of the stem (peduncular white matter) of the cerebellum as shown in Fig. 2C and the other ROI at the dorsomedial aspect of the midbrain. The MCP was tracked by placing two ROIs at the left and right lateral pontine tegmentum, respectively, in a coronal section where a tract compatible with the MCP could be clearly identified on the color map (Fig. 2D). When the coronal slice was placed anterior to the CST level, the tracking often labeled a portion of the CST; therefore, the slice level for MCP delineation was chosen posterior to the CST. For the ICP, one ROI was placed in the lateral aspect of the rostral medulla where it could be discretely identified and the other in the white matter at the stem of the cerebellum as shown in Fig. 2E.

The effect of varying the two thresholds, FA and IP, on the tracking results is also shown in Fig. 2 (middle and right column). For all five tracts, the number of pixels selected decreased with increasing FA threshold. For relatively high FA and IP thresholds of 0.45 and 0.75, respectively, no tracking result was obtained for the MCP due to a low FA region when it crossed the midline. For two other tracts, the SCP and the ICP, the pixel count was also very low for FA $>$ 0.45. When the FA threshold approached that of gray matter (0.15), tracking of the CST, SCP, and ML started to include adjacent tracts, as can be seen in the middle column graph in Fig. 2 (tracking results with FA $>$ 0.15 are shown in red). Inclusion of adjacent tracts is also indicated by asterisks in the right column of Fig. 2. Between the FA threshold of 0.25 and 0.35, the tracking reproduced the same trajectories with respect to length and the only difference was the diameter of the trajectories (the lower the threshold, the larger the diameter). For two tracts, the CST (the tract with least curvature) and the MCP (the tract with steepest curvature), this assessment was repeated with different IP thresholds in a range of 0 (no threshold) $-$0.86. The effect of varying the IP threshold was small for FA $>$ 0.25, indicating that the FA threshold is the more stringent threshold in this range. Nonetheless, the importance of the IP threshold was apparent from the results without it, which showed significantly more contaminated pixels. For example, for the MCP, the IP threshold of 0.86 significantly reduced the number of the pixels (Fig. 2, MCP, the right column).

The tracking of the five major fibers bundles described above was repeated three times by the same operator using different FA (0.15–0.45) and IP thresholds (0.0–0.86). The standard deviations (error bars) of the number of pixels are presented in the right column of Fig. 2, which shows only small variances for an FA threshold higher than 0.25 and an IP threshold higher than 0.5. The low reproducibility with low FA threshold (FA $<$ 0.25) is caused by higher sensitivity of the tracking result to the size of manually drawn ROI because of the inadvertent inclusion of adjacent gray matter and smaller tracts in the ROI. Intra- and interrater reproducibility of the tracking in terms of the κ value is shown in Table 1 for each tract with the FA threshold of 0.25 and 0.35, which indicates "almost perfect" agreement for all tracts ($\kappa > 0.8$).

TABLE 1

The κ Values of Intra- and Interrater Variability for the Five Major Tracts in the Brain Stem

	FA threshold	CST	ML	SCP	MCP	ICP
Intrarater	0.25	1.0	0.931	0.886	1.0	0.972
	0.35	1.0	0.911	0.922	1.0	1.0
Interrater	0.25	0.915	0.888	0.900	0.994	0.982
	0.35	0.966	0.893	0.824	0.996	0.938

Color Maps, 3D Fiber Bundle Tracking, and Comparison with Histology

Figure 3 shows six representative slices of color maps compared to T_2-weighted images and brainstem anatomical preparations. It can first be seen that the DTI-based color maps can delineate a more complex substructure within the white matter than the T_2-weighted images. The brightness of the color maps, which reflects the magnitude of anisotropy, provides high contrast between white matter and gray matter, while the color, which indicates orientation of tracts, differentiates various tracts within the white matter. Comparison with histological preparations (right column, adapted from Williams *et al.* (1997)) demonstrates that some tracts can be discretely identified in the color maps. For example, the corticospinal tract (tract 1) can be clearly delineated in the color maps at the slice levels of Figs. 3B–3D.

The anatomical information on color maps can be further augmented by 3D-trajectory information provided by the reconstructed fibers. Figure 4A shows the results of the automated tracking for the following major brainstem fibers: corticospinal tract (CST, red), medial lemniscus (ML, cyan blue), inferior cerebellar peduncle/spinocerebellar tract (ICP, green), middle cerebellar peduncle (MCP, yellow), and superior cerebellar peduncle (SCP, pink). The tracking results are in high qualitative agreement with standard anatomical postmortem data [Fig. 4B, adapted from Nieuwenhuys *et al.* (1983)]. Figure 3 illustrates two-dimensionally, slice-by-slice, the similarity between tracking overlaid on T_2-weighted images and anatomical data.

Parcellation of Homogeneously Appearing White Matter

Parcellation of the cerebral peduncle, which is known to contain three major fiber systems, the fron-

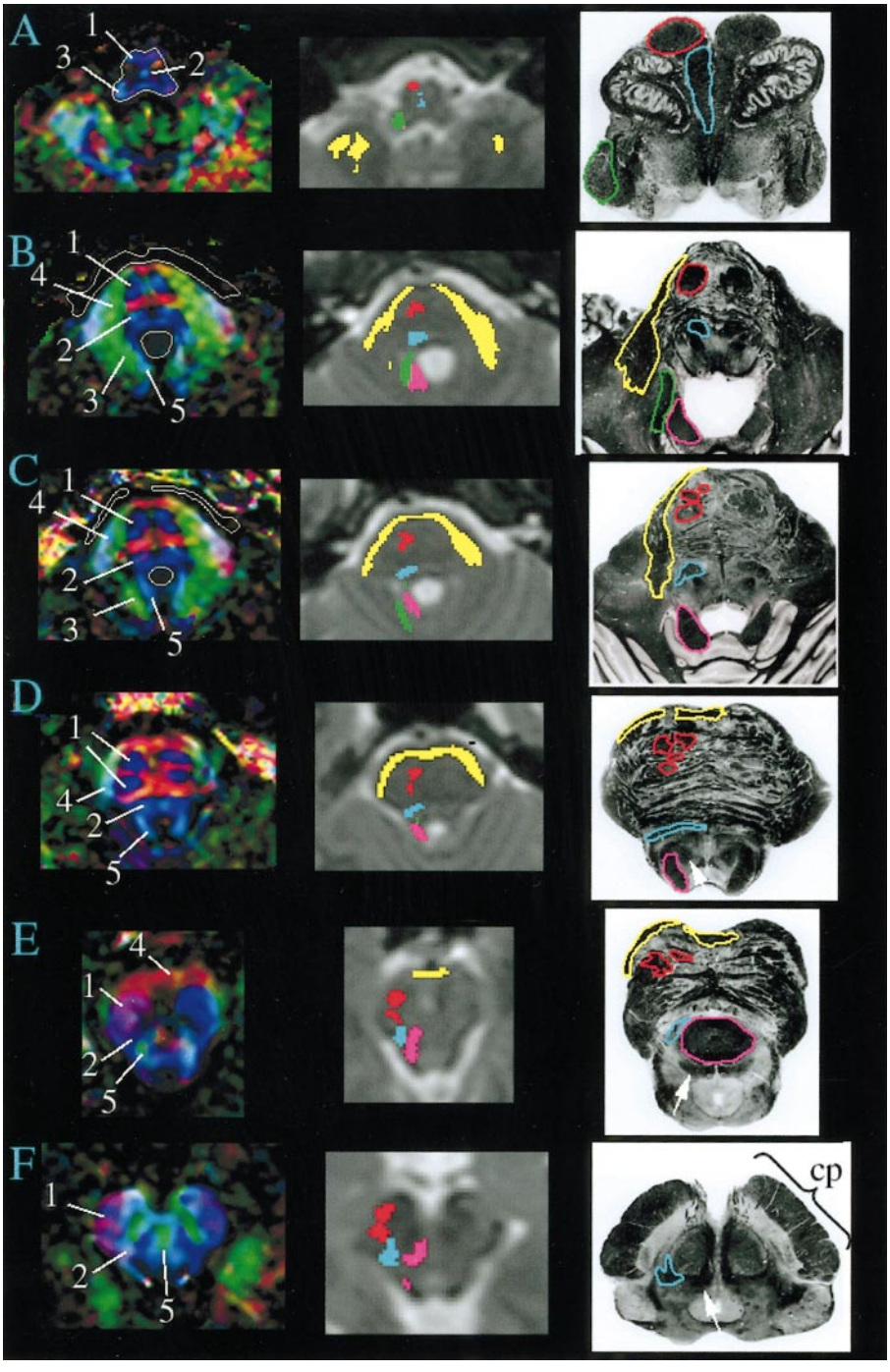

FIG. 3. Comparison of DTI-based color maps, T_2-weighted images, and histology for six slices in the medulla, pons, and midbrain. In the color maps (left column), red represents fibers running in the right–left direction, green ventral–dorsal (anterior–posterior), and blue rostral–caudal (superior–inferior). The intensity is scaled in proportion to the degree of diffusion anisotropy (fractional anisotropy). Numbers in the color maps represent the five major tracts reconstructed in this study. These are 1, corticospinal tract (CST); 2, medial lemniscus (ML); 3, inferior cerebellar peduncle (ICP); 4, medial cerebellar peduncle (MCP); and 5, superior cerebellar peduncle (SCP). Results of 3D tract tracking are superimposed on the T_2-weighted images (second column) using color coding; red, CST; cyan, ML; green, ICP; yellow, MCP; and pink, SCP. Locations of the tracts were also specified on the histology (third column (Williams *et al.* 1997)) using the same color coding. White arrows in D–F indicate the locations of central tagmental tract/medial longitudinal fasciculus. cp, cerebral peduncle.

topontine (FPT), corticospinal, and temporo parietooccipitopontine (TPOPT) tracts, was also attempted (Fig. 5). For this analysis, the first reference ROI was placed to include the entire cerebral peduncle (a yellow box in the left panel of Fig. 5A). Differentiation among these three cerebral peduncle components was then accom-

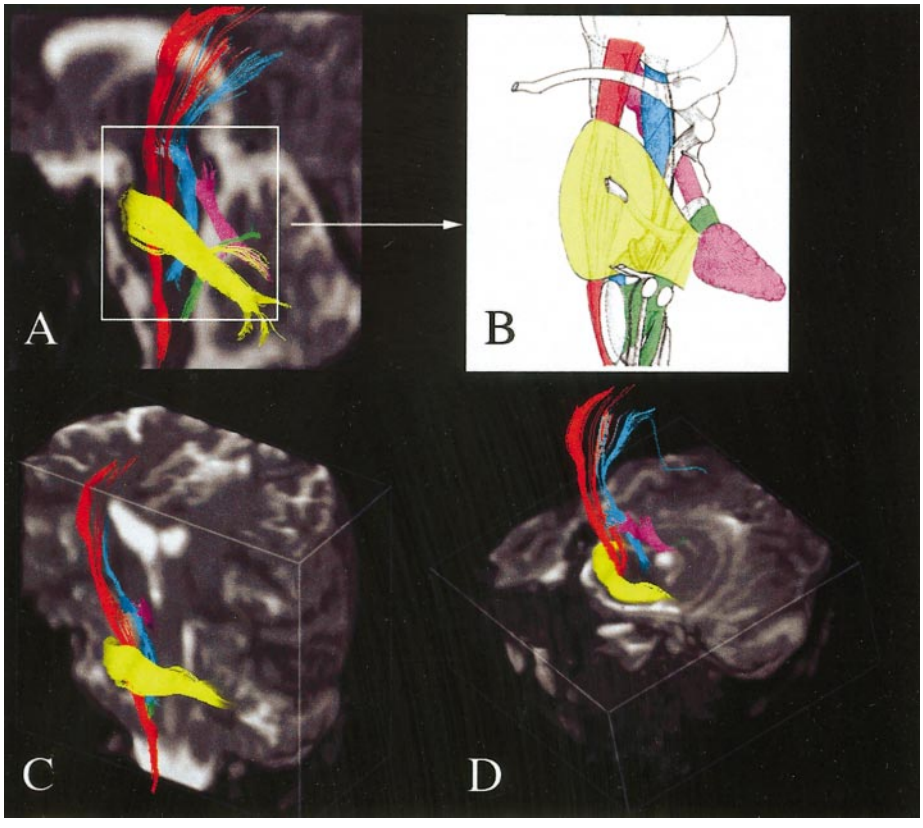

FIG. 4. A three-dimensional view of reconstructed tracts (A) and comparison with postmortem human data (B) (modified from Nieuwenhuys *et al.*, 1983). In (A), tracking results for the white matter bundles are superimposed on a midsagittal T_2-weighted image to match the viewing angle of the postmortem data (B). Color coding is the same as Fig. 3. In (C) and (D), reconstructed tracts are visualized from different view angles.

plished using ROIs at the lower pons level, which only includes the CST (see the second yellow box in the right panel of Fig. 5). A comparison between DTI and other imaging and anatomical modalities is depicted in Fig. 5C. Figure 5C-4 shows the resulting tracking result superimposed on a T_2-weighted image at the level of the cerebral peduncle. In contrast with the homogeneous appearance on DTI anisotropy maps (Fig. 5C-1), white matter staining (Fig. 5C-2), DTI-based color maps (Fig. 5 C-3), and T_2-weighted images (Fig. 5C-4), 3D tracking can dissect the cerebral peduncle into three regions (Fig. 5C-4).

Intersubject Comparison

The tracking protocols discussed above were applied to five additional subjects. The results are shown in Fig. 6 for cross-sections through the medulla, pons, and midbrain levels. The CST (red), ML (cyan blue), SCP (pink), and ICP (green) were reproducibly reconstructed. At the midbrain level, trajectories of the SCP (pink) had small variations and failed to reach the decussation level of SCP for one subject. This medial tegmental region of the rostral brainstem contains several small tracts, such as central tegmental tract and medial longitudinal fasciculus (Fig. 3, white arrows), which, with the current imaging resolution, could not be resolved from the SCP. The MCP forms a thin sheet-like structure at the ventral pontine level that could be well reproduced in five out of six subjects, but only partially reproduced in one subject.

Tract-Specific Quantitative MRI

As seen in Figs. 1–5, DTI analysis provides detailed information on the anatomy of white matter tracts with respect to their locations and trajectories. This capability of delineating individual white matter tracts enabled us to specifically define intrinsic fiber bundle properties using several MRI modalities. To achieve this, we used coregistered MRI data that reflected diffusion properties (FA maps) and water relaxation (T_2 maps). Profiles of FA and T_2 for different tracts along the rostrocaudal (CST, ML, SCP, and ICP) or ventral–dorsal (MCP) axis are illustrated in Fig. 7. These results, averaged over six healthy volunteers, were obtained by normalizing brainstem length based on two anatomical landmarks (upper most rostral and caudal pontine slices). The data indicate that fibers in the brainstem have distinctive anisotropy and T_2 varia-

tions over their trajectories. For example, the CST has progressively increasing anisotropy from the rostral medulla to the caudal midbrain, while its T_2 is reduced at the pons level compared to the medulla and midbrain. Although the SCP has a FA profile that is somewhat similar to that of the CST, it has much longer T_2 in most levels of the pons. The MCP, on the other hand, is featured by short T_2. Figure 8A shows the relationship between T_2 and FA values for different tracts at the pons level. These characteristic T_2 properties of each tract can be also clearly appreciated from the FA and T_2 maps shown in Fig. 8B. Regression analysis between the two parameters for each tract within the brainstem results in $R^2 = 0.210$ (CST), 0.056 (ML), 0.092 (SCP), 0.148 (MCP), and 0.152 (ICP) indicating little to no correlation. Delineation of fiber bundles also allowed estimates of their size. For example, the slice-by-slice cross-sectional area of the CST for two separate scan sessions on the same subjects is shown in Fig. 9. It can be seen that the CST decreases in size along the rostral–caudal axis. Relatively large deviations outside the two ROIs were observed, which are due to less constraint in the tracking and the fact that the CST changes rapidly in size in these regions.

DISCUSSION

The DTI results for the human brainstem in Figs. 1–9 and Table 1 show the high sensitivity and validity of a combined DTI color map–fiber tracking for delineating and characterizing major fiber bundles. The fiber tracking results show that the CST, ML, SCP, MCP, and ICP can be reliably mapped using DTI based on the thresholds defined in the previous section (FA = 0.25–0.35 and IP = 0.75). Qualitative comparison with postmortem human data shows excellent agreement between the *in vivo* DTI and anatomical data, thereby validating the fiber-tracking DTI approach. Individual tracts were shown to have specific signatures in terms of T_2 relaxation and fiber anisotropy variation over the brainstem. In view of these results it is important to discuss the relative advantages of using 2D color map and 3D tracking approaches and the effect of appropriate choice of image plane, spatial resolution, reference ROIs, and tracking thresholds. In addition, the finding of negligible correlation between the tract-specific relaxation and anisotropy needs to be assessed.

Characterization of Fiber Bundles by 2D Color Maps and 3D Fiber Tract Reconstruction

Among anatomic components of the CNS, the brainstem is characterized by its relatively simple white matter architecture. Moreover, the trajectories of most major brainstem fiber bundles have been well defined by conventional postmortem anatomical techniques. For these reasons, in addition to its clinical importance, we consider the brainstem a particularly suitable region for evaluating the feasibility and validity of novel DTI analyses. Two-dimensional color maps could be used to delineate several of the major brainstem tracts at levels in which conventional imaging techniques, and even standard neuroanatomical preparations, are largely unrevealing. The usefulness of color maps has been previously demonstrated for the brainstem and other CNS regions by Makris *et al.* (1997) and Pajevic and Pierpaoli (1999). Slice-by-slice identification of a particular tract in color maps is, however, not always straightforward due to the existence of adjacent fibers with a similar color (orientation) or due to changes in color as the tract changes direction within or through slices. Therefore, to identify the trajectories of tracts of interest unambiguously, computer-aided tracking was highly beneficial. This point was demonstrated in Fig. 5, in which the locations of the CST, FPT, and FPOPT were identified within the homogeneous-looking cerebral peduncle. Another example is the medial cerebellar peduncle (MCP, Figs. 3B–3D), for which the color transition (green–red–green) in the color maps may potentially suggest that it has a U-shape trajectory around the pons within the axial plane. However, our 3D tracking results and postmortem studies (Fig. 4) show that the actual trajectory of the MCP is significantly tilted in the dorsal–ventral axis especially at the superior part of the pons, which is very difficult to appreciate from color maps.

Methodological Limitations for Tracking

Data acquisition. For 3D fiber tracking using the FACT approach, several factors influence the results. The most notable are the choice of image plane and the in-plane spatial resolution. These choices influence the magnitude of the partial volume effect between image pixels, which is the result of limitations in resolution (voxel $2 \times 2 \times 3$ mm, resolution-enhanced or zerofilled to $1 \times 1 \times 3$ mm). One practical and effective way to reduce this problem is to use an imaging plane perpendicular to the orientation of tracts of interest, which is especially practical in the brainstem, where partial volume effects caused by the thick slice (3 mm) are not detrimental. Choice of in-plane resolution is determined by practical considerations such as available signal-to-noise ratio (SNR) and sensitivity to bulk motion. These two highly related issues (resolution and SNR) really depend on the sizes of tracts of interest, because white matter tracts that are smaller than the pixel size cannot be reliably reconstructed. This means that the appropriate tracking protocol (locations of ROIs and choice of thresholds) may differ for each white matter tract and specific resolution and SNR.

Data processing. In view of these limitations in data acquisition, we focused first on only the well-documented large white matter tracts and employed a

multiple-ROI approach that is based on existing anatomical knowledge. If only one ROI were used, the result would be highly susceptible to the partial volume and noise effects or contamination by merging or closely located parallel tracts. However, by using multiple ROIs, tracking results that deviate from the real trajectory are not likely to penetrate other ROIs by chance, thus, increasing the accuracy of the resulting fiber location. The comparison between tracking results and anatomical data indicate that this is indeed the case. One disadvantage of this approach is that branching patterns of tracts of interest between the two reference ROIs cannot be studied. While this approach may sometimes preclude the study of anatomically not well-described trajectories (i.e., for cases where two anatomical landmarks can not be specified), this approach can still be applied to brains with deformed anatomy as long as an appropriate set of reference ROIs can be chosen. An example of such a situation is given in Fig. 10, for a patient with a brainstem meningioma, where the tracts have been pushed outside the normal area in the brainstem region. The two anatomical landmarks for the CST described in Fig. 2 could not be discretely identified in this patient. However, it was still possible to track the CST by choosing two new appropriate ROIs, one at the medulla and the other at the posterior limb of the internal capsule, which were both outside the deformed areas and thus could be easily identified.

It should be clear from Fig. 2 that, in addition to the choice of reference ROIs, the tracking results depend on two other subjective parameters chosen by raters, namely, the FA and IP thresholds that determine the termination of fiber tracking. Examination of the effects of these thresholds (Fig. 2) showed that a FA threshold equivalent or lower than the upper gray matter FA limit (0.15) induced significant levels of contamination in three of the five tracts when using the IP threshold of 0.75 (CST, SCP, and ML). On the other hand a FA threshold higher than 0.45 was too stringent for the three cerebellar peduncles. When using a FA threshold of between 0.25 and 0.35, the effect of the IP threshold was minimal over the 0.5–0.86 range. Based on these analyses, we recommend the use of FA between 0.25–0.35 and an IP of 0.75 for our present resolution and SNR. With the ROI placement protocol and suggested FA/IP thresholds described above, intra- and interrater reliability and tract configuration agreement among the six studies subjects for the five major tracts were excellent (see Table 1, Fig. 6).

In addition to the five fibers that could be reproducibly tracked in this study, we could identify portion of other smaller tracts at some limited slice levels. These were the MLF and CTT (see Figs. 1 and 3). However, these tracts were not large enough to be reliably reconstructed at the imaging resolution used in this study. The computational time for the exhaustive search of tracts that penetrate the two ROIs was about 5–10 min with FA $>$ 0.35 and 10–15 min with FA $>$ 0.25 using an 866 MHz Pentium III processor.

Tract-Specific MRI Studies

The information of the 3D tract trajectories was superimposed on coregistered MR images, allowing the measurement of tract-specific MRI parameters along a fiber bundle (Xue *et al.*, 1999; Virta *et al.*, 1999). It should be noted that measured FA values depend on FA threshold used for the fiber tracking. If a lower FA threshold is used for tracking, more marginal regions of the tract are included in the tracking results, leading to lower average FA values for the tract. In Fig. 7, FA and IP thresholds of 0.25 and 0.75, respectively, were used for the tracking. When FA $>$ 0.35 was used, average FA values of each tract increased by approximately 0.05. On the other hand, the characteristic profiles of the FA and T_2 of each tract as a function of position were preserved regardless of the FA threshold (0.25–0.35). When correlating the FA and T_2 data for the individual tracts, no correlation was found. This is an important result in terms of understanding fiber properties and the origin of anisotropy. Anisotropy has been postulated to be related to the degree of fiber organization, which could reflect both axonal and myelin influences, although recent work by Beaulieu and Allen suggests a predominantly axonal origin (Beaulieu and Allen, 1994). T_2, on the other hand, has been related to myelin water content (MacKay *et al.*, 1994; Stanisz *et al.*, 1999). As a consequence, the profiles in Fig. 7 may thus reflect the unique architecture of each fiber in terms of axon-to-myelin ratio. The data indicate that these MRI parameters can vary along the fiber pathway trajectory as well. However, at the present resolution care has to be taken in directly interpreting the data in terms of axon and myelin contributions because of tracts that may be bending, crossing, merging, and fanning. Nonetheless, this tract-specific approach has the potential to increase the sensitivity and specificity of analyses of white matter lesions.

Continued Tracking of Brain Stem Fibers into the Cerebrum

Tracking of the CST showed its trajectories not only in the brainstem but also in the cerebral hemispheres (Figs. 1, 4, and 5). Portions of two other tracts, SCP and ML reached the thalamus, after which some fibers continued to project from the thalamus to the corona radiata and to cortical areas. While these axonal projections into the cerebrum are of great interest, care must be taken to interpret these tracking results because they lie outside of the region selected by the two reference ROIs. As a consequence, these results are more susceptible to noise and partial volume effects,

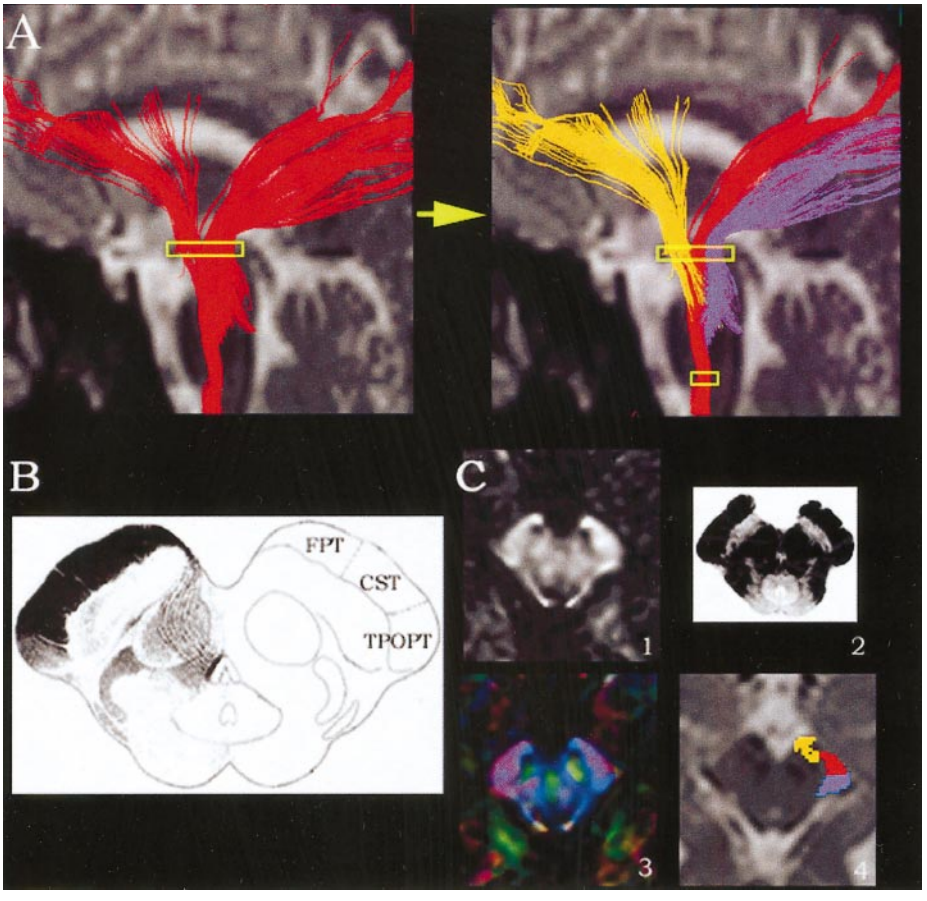

FIG. 5. Parcellation of the cerebral peduncle. If one reference ROI is defined at the cerebral peduncle (indicated by a yellow box in the left panel of (A)), multiple tracts penetrating the cerebral peduncle are reconstructed. By adding the second ROI at the lower pons level (smaller yellow box in the right panel of (A)), only the CST is selected based on the knowledge that the CST penetrates both ROIs. The fibers anterior and posterior to the CST are the frontopontine (FPT, indicated by orange) and temporo-/parieto-/occipitopontine (TPOPT, purple) tracts, respectively. (B) A cross-section of the pons (modified from Carpenter, 1976) shows the proposed separation of the cerebral peduncle (black wing on the left side) as based on acquired lesions and tracer studies in primates. The three regions are separated by dotted lines. (C) Images of the cerebral peduncle using various methods: (1) anisotropy map, (2) white matter staining, (3) DTI-based color map, and (4) 3D tracking superimposed on a T_2-weighted image.

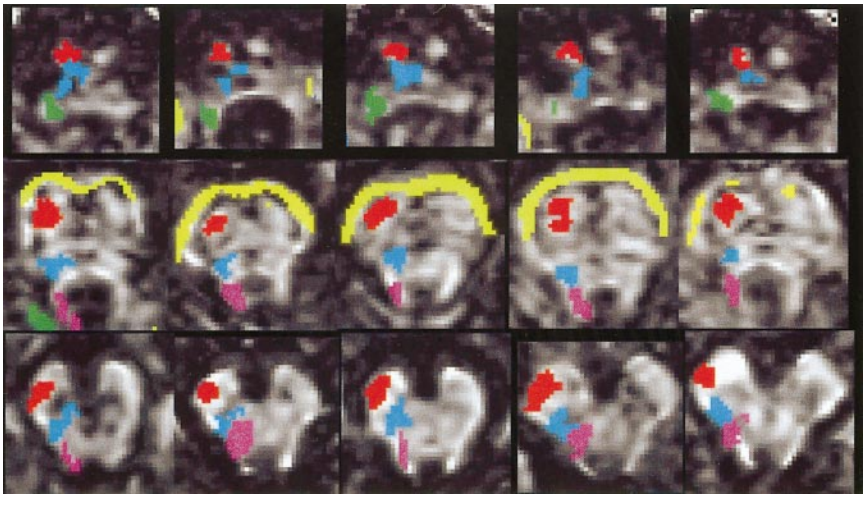

FIG. 6. Tracking results of the five major tracts in the five other volunteers at three different slice levels (the medulla, pons, and midbrain). Tracking was performed using the FA threshold of 0.35 and IP threshold of 0.75 except for the MCP for which a FA threshold of 0.25 was used. Color coding is as in Fig. 3.

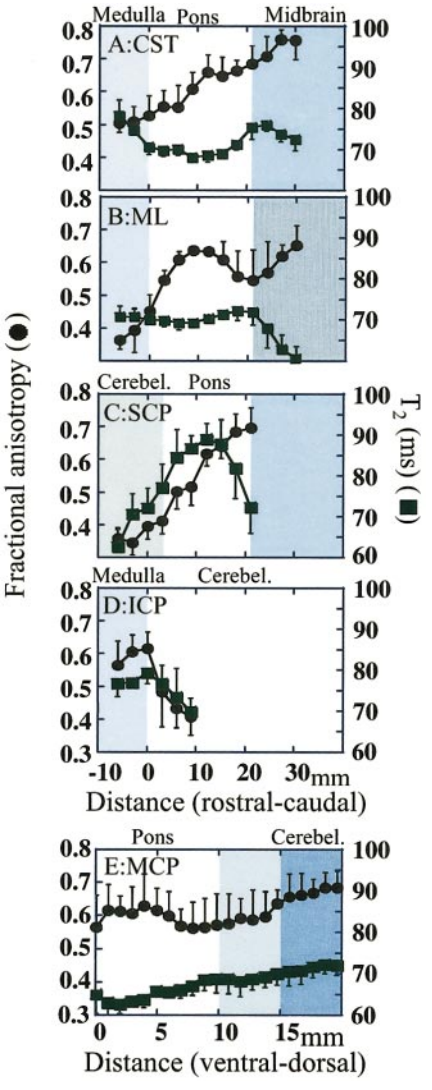

FIG. 7. Tract-specific determination of water diffusion anisotropy (FA) and T_2 for the CST (A), ML (B), SCP (C), ICP (D), and MCP (E), obtained using a FA threshold of 0.25 and an IP threshold of 0.75. FA and T_2 values are plotted along the rostral–caudal axis (0 represents the beginning of the pons) except for MCP, which is plotted along the ventral–dorsal axis (0 represents the ventral end of the pons). Data show the average of six subjects ± SD.

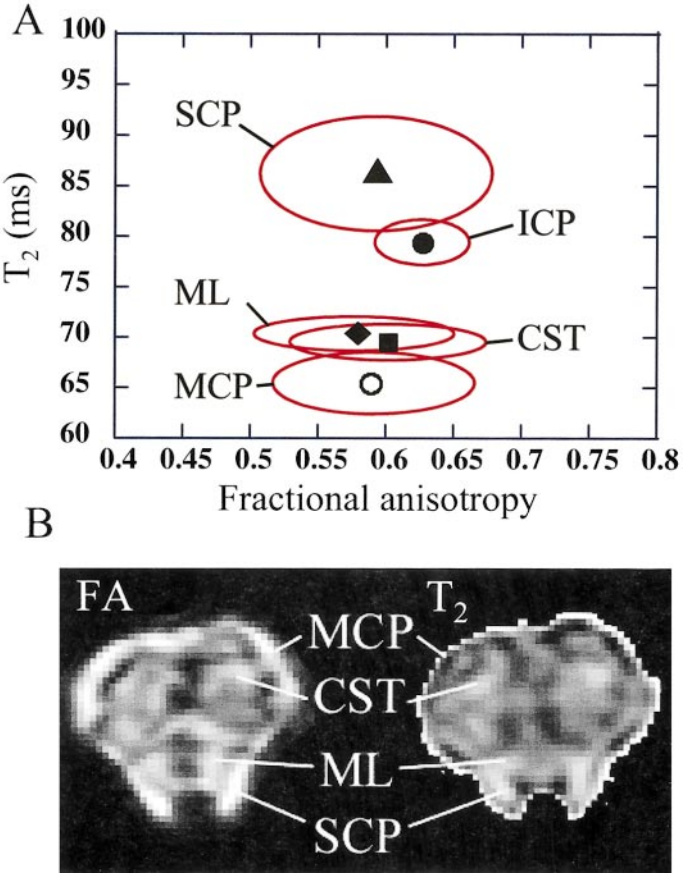

FIG. 8. Correlation between FA and T_2 of each tract at the pons level (A) and images of FA (left) and T_2 (right) maps at a slice of the pons level (B). Abbreviations are as in Fig. 1.

and, as such, have high sensitivity to threshold choice, as can be appreciated from Fig. 2. Further complications arise due to the lack of precise anatomical knowledge on the trajectories of these fibers in the cerebral hemisphere (Crick and Jones, 1993). Because of these factors, we did not analyze these cerebral regions here. On the other hand, this study developed principles for applying the same approach to the cerebral hemispheres. By using the two-ROI approach, the FA threshold of 0.25–0.35, and the IP threshold of higher than 0.75, identified trajectories by the FACT technique are likely to be valid. In addition, promising techniques were proposed recently that can reduce the deleterious effects of noise and partial volume effects (Poupon *et al.*, 2000). Various improvements in scanning (e.g., higher field and higher gradient strength) and acquisition techniques (e.g., real-time navigator echo monitoring) that are expected to provide better

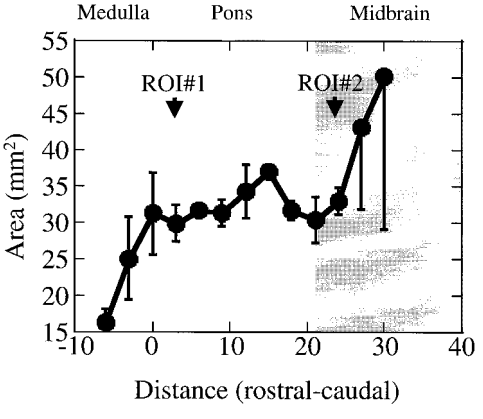

FIG. 9. Cross-sectional areas of the CST along the rostral–caudal axis determined from the number of pixels labeled by the automatic tracking technique. Results are the averages and standard deviations of two separate measurements on the same subject.

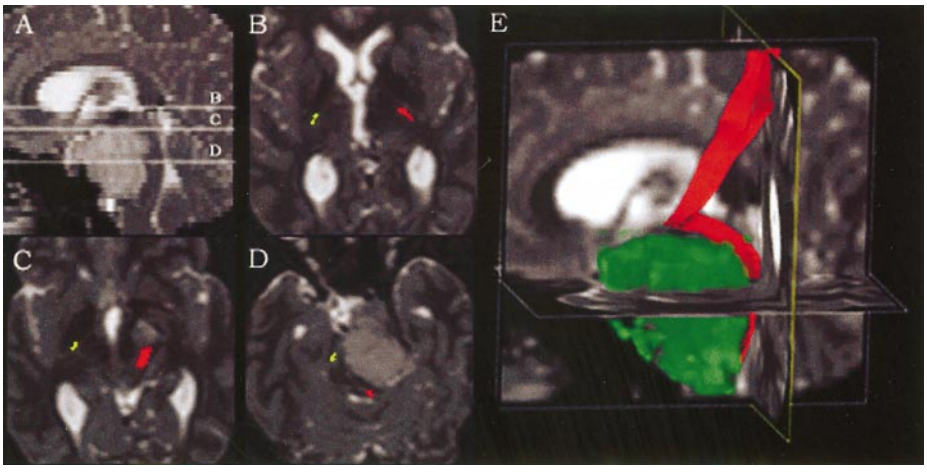

FIG. 10. Deformation of the corticospinal tract in a patient with a meningioma. (A) Midsagittal T_2-weighted image showing the extent of the tumor. (B–D) T_2-weighted axial images with superimposed the left (yellow) and right (red) corticospinal tract. The section level is indicated on (A). (E) Triplanar view of the tumor rendered in green and the right CST in red.

resolution and SNR are under development and should further reduce the variability of tracking results.

In summary, using a combination of high-resolution *in vivo* DTI methods and analyses, we were able to delineate and reconstruct several major brainstem tracts in agreement with standard neuroanatomical knowledge. These 3D data provided greater information about white matter composition than conventional MRI sequences. Specifically, we delineated white matter tracts in 2D and 3D spaces (Figs. 1–4) and parcellated homogeneous white matter into different components using the information of 3D trajectories (Fig. 5). Analyses using coregistered images demonstrated the feasibility of combining DTI with other MRI modalities, providing information on tract-specific properties such as anisotropy, T_2, and cross-sectional area (Figs. 7–9).

Because the brainstem has a relatively simple and well-defined white matter architecture, which has been documented by anatomical data, our study could demonstrate the feasibility and validity of applying DTI color maps and automated fiber tracking-based analyses. As such, these results provide a basis for applying this technology to other brain areas, where this information is not available.

ACKNOWLEDGMENTS

This work was supported in part by the Whitaker Foundation (S.M.), the Shapiro Foundation (G.D.P.), and National Institutes of Health Grants AG016028 (S.M.), HD37931 (S.M.), HD24061 (W.E.K), and MH52886 (G.D.P.). We acknowledge Ms. Terry Brawner (F. M. Kirby Research Center at Kennedy Krieger Institute) and Dr. Paul Folkers (Philips Medical Systems) for technical assistance and Drs. Paul Bottomley (Johns Hopkins University), Laura Amodei (Johns Hopkins University), and Gary Goldstein (Kennedy Krieger Institute) for critically reviewing the manuscript. Machine time for these studies was provided by the F. M. Kirby Research Center for Functional Brain Imaging at the Kennedy Krieger Institute.

REFERENCES

Basser, P. J., Mattiello, J., *et al.* 1994a. MR diffusion tensor spectroscopy and imaging. *Biophys. J.* **66:** 259–267.

Basser, P. J., Mattiello, J., *et al.* 1994b. Estimation of the effective self-diffusion tensor from the NMR spin echo. *J. Magn. Reson. B* **103:** 247–254.

Basser, P. J., Pajevic, S., *et al.* 2000. In vitro fiber tractography using DT-MRI data. *Magn. Reson. Med.* **44:** 625–632.

Beaulieu, C., and Allen, P. S. 1994. Determinants of anisotropic water diffusion in nerves. *Magn. Reson. Med.* **31:** 394–400.

Carpenter, M. 1976. *Human Neuroanatomy.* Williams & Wilkins, Baltimore.

Conturo, T. E., Lori, N. F., *et al.* 1999. Tracking neuronal fiber pathways in the living human brain. *Proc. Natl. Acad. Sci. USA* **96:** 10422–10427.

Coremans, J., Luypaert, R., *et al.* 1994. A method for myelin fiber orientation maping using diffusion-weighted MR images. *Magn. Reson. Imag.* **12:** 443–454.

Crick, F., and Jones, E. 1993. Backwardness of human neuroanatomy. *Nature* **361:** 109–110.

Douek, P., *et al.* 1991. MR color mapping of myelin fiber orientation. *J. Comput. Assist. Tomogr.* **15:** 923–929.

Henkelman, R., Stanisz, G., *et al.* 1994. Anisotropy of NMR properties of tissues. *Magn. Reson. Med.* **32:** 592–601.

Landis, J. R., and Koch, G. G. 1977. The measurement of observer agreement for categorical data. *Biometrics* **33:** 159–174.

MacKay, A., Whittall, K., *et al.* 1994. In vivo visualization of myelin water in brain by magnetic resonance. *Magn. Reson. Med.* **31:** 673–677.

Makris, N., Worth, A. J., *et al.* 1997. Morphometry of in vivo human white matter association pathways with diffusion weighted magnetic resonance imaging. *Ann. Neurol.* **42:** 951–962.

Mori, S., Crain, B. J., *et al.* 1999. Three dimensional tracking of axonal projections in the brain by magnetic resonance imaging. *Ann. Neurol.* **45:** 265–269.

Mori, S., Kaufmann, W. K., *et al.* 2000. *In vivo* visualization of human neural pathways by MRI. *Ann. Neurol.* **47:** 412–414.

Mori, S., and van Zijl, P. C. M. 1995. Diffusion weighting by the trace of the diffusion tensor within a single scan. *Magn. Reson. Med.* **33:** 41–52.

Moseley, M. E., Cohen, Y., *et al.* 1990. Diffusion-weighted MR imaging of anisotropic water diffusion in cat central nervous system. *Radiology* **176:** 439–445.

Nakada, T., and Matsuzawa, H. 1995. Three-dimensional anisotropy contrast magnetic resonance imaging of the rat nervous system: MR axonography. *Neurosci. Res.* **22:** 389–398.

Nieuwenhuys, R., Voogd, J., *et al.* 1983. *The Human Central Nervous System.* Springer-Verlag, Berlin.

Ordidge, R. J., Helpern, J. A., *et al.* 1994. Correction of motional artifacts in diffusion-weighted NMR images using navigator echoes. *Magn. Reson. Imag.* **12:** 455–460.

Orioli, P., and Strick, P. 1989. Cerebellar connections with the motor cortex and the arcuate premoter area: An analysis employing retrograde transneuronal transport of WGA-HRP. *J. Comp. Neurol.* **22:** 612–626.

Pajevic, S., and Pierpaoli, C. 1999. Color schemes to represent the orientation of anisotropic tissues from diffusion tensor data: Application to white matter fiber tract mapping in the human brain. *Magn. Reson. Med.* **42:** 526–540.

Pierpaoli, C., and Basser, P. J. 1996. Toward a quantitative assessment of diffusion anisotropy. *Magn. Reson. Med.* **36:** 893–906.

Pierpaoli, C., Jezzard, P., *et al.* 1996. Diffusion tensor MR imaging of human brain. *Radiology* **201:** 637–648.

Poupon, C., Clark, C. A., *et al.* 2000. Regularization of diffusion-based direction maps for the tracking of brain white matter fascicules. *NeuroImage* **12:** 184–195.

Stanisz, G., Kecojevic, A., *et al.* 1999. Characterizing white matter with magnetization transfer and T2. *Magn. Reson. Med.* **42:** 1128–1136.

van Gelderen, P., de Vleeschouwer, M. H., *et al.* 1994. Water diffusion and acute stroke. *Magn. Reson. Med.* **31:** 154–163.

Virta, A., Barnett, A., *et al.* 1999. Visualizing and characterizing white matter fiber structure and architecture in the human pyramidal tract using diffusion tensor MRI. *Magn. Reson. Imag.* **17:** 1121–1133.

Williams, T. H., Gluhbegovic, N., *et al.* 1997. The Human Brain: Dissections of the Real Brain. *Virtual Hospital, University of Iowa,* http://www.vh.org/Providers/Textbooks/BrainAnatomy.

Woods, R. P., Cherry, S. R., *et al.* 1992. Rapid automated algorithm for aligning and reslicing PET images. *J. Comput. Assist. Tomogr.* **16:** 620–633.

Xue, R., van Zijl, P. C. M., *et al.* 1999. In vivo three-dimensional reconstruction of rat brain axonal projections by diffusion tensor imaging. *Magn. Reson. Med.* **42:** 1123–1127.

Yaginuma, H., and Matsushita, M. 1989. Spinocerebellar projections from the upper lumbar segments in the cat, as studied by anterograde transport of wheat germ agglutinin-horseradish peroxidase. *J. Comp. Neurol.* **281:** 298–319.